

Superior energy storage capacity of polymer-based bilayer composites by introducing 2D ferroelectric micro-sheets

Received: 24 August 2024

Accepted: 2 December 2024

Published online: 30 January 2025



Zhenhao Fan¹, Jian Dai¹, Yuyan Huang², Hang Xie¹, Yitao Jiao³, Wenfeng Yue¹, Fu Huang¹, Yuqun Deng¹, Dawei Wang^{1,4}✉, Qingfeng Zhang²✉ & Yunfei Chang^{1,4}✉

Dielectric polymer capacitors suffer from low discharged energy density and efficiency due to their low breakdown strength, small dielectric constant and large electric hysteresis. Herein, a synergistic enhancement strategy is proposed to significantly increase both breakdown strength and dielectric constant while suppressing hysteresis, through introducing 2-dimensional bismuth layer-structured $\text{Na}_{0.5}\text{Bi}_{4.5}\text{Ti}_4\text{O}_{15}$ micro-sheets and designing a unique bilayer structure. Excitingly, an ultra-high discharged energy density of 25.0 J cm^{-3} and a large efficiency of 81.2% are achieved in $\text{Na}_{0.5}\text{Bi}_{4.5}\text{Ti}_4\text{O}_{15}$ -poly(vinylidene fluoride-co-hexafluoropropylene)/ $\text{Na}_{0.5}\text{Bi}_{4.5}\text{Ti}_4\text{O}_{15}$ -polyetherimide bilayer composites under a dramatically enhanced breakdown strength of 8283 kV cm^{-1} . Finite element simulations along with experimental test results demonstrate that greatly improved breakdown strength is ascribed to uniform and horizontal alignments of $\text{Na}_{0.5}\text{Bi}_{4.5}\text{Ti}_4\text{O}_{15}$ sheets ($\sim 1\text{--}2 \mu\text{m}$) in the matrix and interface effect of adjacent layers with large dielectric differences, which effectively inhibit electrical tree evolution and conduction loss. This work provides a strong foundation for developing high-performance polymer-based energy storage devices.

In recent years, dielectric capacitors have played a critical role in advanced electronic power systems and energy storage devices, owing to their rapid charge-discharge characteristics and remarkable power density^{1–5}. Polymer-based dielectric capacitors are highly attractive to researchers because of their high E_b , low mass, stable structure, and good flexibility. However, low energy storage density compared with batteries and super capacitors limits their broad use in the energy storage device market. To improve their discharged energy density (U_{dis}), it is essential to improve the breakdown strength (E_b) and dielectric constant (ϵ_r) of their dielectric components according to the

follow equation^{6,7}:

$$U_{\text{dis}} = \frac{1}{2} \epsilon_0 \epsilon_r E_b^2 \quad (1)$$

where ϵ_0 is the permittivity of vacuum ($8.85 \times 10^{-12} \text{ F m}^{-1}$)². In this context, filling 2D dielectric materials including boron nitride nanosheets (BNNS)⁸, $\text{Ca}_2\text{Nb}_3\text{O}_{10}$ ⁹, Mxene¹⁰ and montmorillonite (MMT)¹¹ into the polymer matrix is a valid method to enhance the tortuosity of conductive pathways at large electric fields, thereby improving the E_b of the composites. For instance, Li et al.⁸ reported

¹School of Instrumentation Science and Engineering, Harbin Institute of Technology, Harbin, China. ²School of Materials Science and Engineering, Hubei University, Wuhan, China. ³Institute of Applied Physics and Materials Engineering, University of Macau Avenida da Universidade, Taipa, Macau, China.

⁴Zhengzhou Research Institute, Harbin Institute of Technology, Zhengzhou, China. ✉e-mail: wangdawei102@gmail.com; zhangqingfeng@hubu.edu.cn; changyunfei@hit.edu.cn

that adding 12 vol% BNNS to poly(vinylidene fluoride-trifluoroethylene-chlorofluoroethylene) (P(VDF-TrFE-CFE)) terpolymers greatly improved the E_b from 4000 to 6500 kV cm⁻¹. Bao et al.^{9,12} obtained a significantly enhanced E_b of 7920 kV cm⁻¹ in PVDF-based nanocomposite capacitors by adding negatively charged Ca₂Nb₃O₁₀ nanosheets. Unfortunately, the ϵ_r of commonly used 2D materials, such as BNNS (–3–4)⁸, is relatively low, which is not helpful for improving the ϵ_r of composites, resulting in a relatively low U_{dis} . Moreover, the widely used PVDF-based composites possess a low energy storage efficiency (η) of ~60%, which means that much energy is lost and converted into heat, being harmful for long-term operation. Therefore, developing dielectric energy storage materials with simultaneously high U_{dis} and η remains a challenge.

After comprehensive consideration, a type of bismuth layer-structured ferroelectric material (Na_{0.5}Bi_{4.5}Ti₄O₁₅, NBT) with simultaneously high ϵ_r and low dielectric loss ($\tan \delta$) has attracted our attention^{13–17}, and more importantly, the charge distribution within 2D layers of Na_{0.5}Bi_{4.5}Ti₄O₁₅ is more uniform than that in other bismuth layer-structured materials (e.g., Bi₄Ti₃O₁₂ and SrBi₂Ta₂O₉), facilitating the achievement of large E_b ^{18,19}. Uniform and flat micro-sized NBT sheets prepared via the molten salt method have been proved to be a potential 2D functional material²⁰. Interestingly, by optimizing the molten salt method process, a specific, dimensionally homogeneous 2D NBT ferroelectric with a size of ~1–2 μ m can be achieved, which could be suitable as a filler with the large faces aligned perpendicular to the direction of the applied electric field, thus forming a barrier to block the passage of electrons to increase the E_b ²¹. Finite element simulations (Supplementary Fig. 1) demonstrate the advantages of the NBT sheets (1–2 μ m) in increasing the E_b of polyetherimides (PEI) polymers relative to BNNS nanosheets (~100 nm) and NBT sheets with a size of ~20 μ m. Owing to small size, BNNS are prone to irregular motion due to Brownian motion, leading to a chaotic distribution in the polymer matrix²². In contrast, the NBT sheets with sizes of 1–2 μ m and ~20 μ m can be aligned with the biggest faces parallel to each other in the matrix. Consequently, the BNNS exhibit the slight blocking effect on electrical tree evolution, and the NBT sheets with the large size (~20 μ m) are directly penetrated by the electrical tree. Excitingly, the 2D NBT sheets with the size of 1–2 μ m effectively serve barriers that impede the direct penetration of electrical trees, making it a very promising candidate for improving E_b .

In addition, multilayer composites, consisting of high E_b and large- ϵ_r layers have demonstrated the ability to integrate the merits of each functional layer effectively. The interface effect, including the Maxwell–Wagner–Sillars (MWS) effect, appears in heterogeneous systems and is favored when the electrical characteristics (e.g., ϵ_r , electron affinity, and band gap) of the constituent phases significantly vary^{23–28}. Poly(vinylidene fluoride-co-hexafluoropropylene) (P(VDF-HFP)) is a potential candidate for capacitor applications due to its high ϵ_r (~9)²⁹. However, P(VDF-HFP)-based composites usually exhibit low η (<60%) when applied in high electric fields. In contrast, linear dielectric PEI exhibits a high E_b (~5000 kV cm⁻¹), an extremely low residual polarization (D_r) and a high η (>90%), but a low ϵ_r (~3)^{30–32}. Therefore, constructing multilayer structure may be a valid method to enhance the capacitive performance.

Herein, we propose a synergistic enhancement strategy to obtain large energy density and efficiency in the NBT-PEI/NBT-P(VDF-HFP) bilayer-structured composite film through incorporation of 2D bismuth layer-structured NBT ferroelectric micro-sheets, as shown in Fig. 1. Interestingly, by combining the electric barrier effect of 2D NBT sheets and the interface effect of the bilayer structure (Fig. 1a, d), an ultra-high U_{dis} of 25.0 J cm⁻³, accompanied by a large η of 81.2% is achieved at an ultra-high E_b of 8283 kV cm⁻¹, which far exceeds those of most reported energy storage materials. In addition, the composite film has excellent actual charge-discharge capacity, exhibiting an extremely fast discharge time of 46.6 ns and an ultra-high-power

density of 62.2 MV cm⁻³, making it a potential material for utilization in high-power devices.

Results and discussion

NBT sheets and bilayer-structured composite films quality

Figure 2a indicates that the X-ray diffraction (XRD) pattern of the NBT sheets matches that of the standard Na_{0.5}Bi_{4.5}Ti₄O₁₅ (PDF#74-1316), which proves that these sheets have a bismuth layered structure. Figure 2b, c presents scanning electron microscopy (SEM) and energy-dispersive spectroscopy (EDS) mapping images of a 2D NBT sheet. Owing to its bismuth layered structure, it has a platelet shape with the size around 1–2 μ m and the Bi, Na, Ti, and O constituents are uniformly distributed overall. The thickness of an NBT sheet is approximately 257 nm, as shown in Fig. 2d. Its high-aspect-ratio platelike shape is beneficial for parallel alignment and uniform dispersion in the polymer matrix, which can be observed from the surface SEM images of the bilayer-structured NBT-PEI/NBT-P(VDF-HFP) composite film (Fig. 2e) and the NBT-PEI and NBT-P(VDF-HFP) composite films with various NBT filler contents (Supplementary Figs. 2 and 3). Obviously, the NBT sheets are uniformly distributed in the polymer matrix without aggregation at low filler contents (<0.75 wt.%), which is helpful for forming a barrier to prevent electrons from passing through when applied in a high electric field. However, the aggregation appears when the filler content exceeds 0.75 wt.%, which can easily lead to local electric field distortion, decreasing E_b of the composite films. Figure 2f shows a macroscopic digital photograph of the NBT-PEI/NBT-P(VDF-HFP) bilayer composite film. The film demonstrates good flexibility, curves in its natural state and is ideal for deformation as conditions change. Figure 2g shows the focused ion beam (FIB)-SEM image of the cross-section of the NBT-PEI/NBT-P(VDF-HFP) composite film. There is a clear demarcation between layers, and the composite films have an overall thickness of 7.7 μ m. In addition, in order to distinguish the components of the different layers, EDS mapping images of the PVDF-specific element F and the PEI-specific element O are shown in Fig. 2h, i. F and O are uniformly dispersed in the top and bottom layers, respectively, suggesting the good homogeneity of the bilayer-structured composite films.

Energy storage performance optimization of composite films

The dependence of the ϵ_r of the 2D NBT sheets on the frequency at room temperature shows that the sheets have a high ϵ_r of 119.0 at 1 kHz (Supplementary Fig. 4). The dielectric and capacitive performances of the NBT-PEI and NBT-P(VDF-HFP) composites with various contents of NBT fillers (Supplementary Figs 5 and 6 and Supplementary Tables 1 and 2) show that the ϵ_r values of the NBT-PEI and NBT-P(VDF-HFP) composites notably increase with increasing content of the NBT filler because of its higher ϵ_r relative to those of PEI and P(VDF-HFP) while the $\tan \delta$ values of the composites are low. Additionally, the ϵ_r of the NBT-P(VDF-HFP) composite films reduces with increasing frequency because the polar groups in P(VDF-HFP) cannot keep up with the movement at high frequencies. When the NBT filler content is 0.75 wt.%, the NBT-PEI composite film displays the largest E_b of 7484 kV cm⁻¹ and the largest D_{max} - D_r value of 4.53 μ C cm⁻², resulting in a maximum U_{dis} of 16.7 J cm⁻³, accompanied by a high η of 92.3%. Compared with that of pristine PEI (U_{dis} = 8.2 J cm⁻³), the U_{dis} of the NBT-PEI composite film is enhanced by 104%. Moreover, for the NBT-P(VDF-HFP) composite film, at a 0.75 wt.% NBT sheet filler content, it presents the largest E_b of 6084 kV cm⁻¹ and the largest D_{max} - D_r value of 6.30 μ C cm⁻², possessing a maximum U_{dis} of 15.5 J cm⁻³, accompanied by a η of 62.4%. Compared with that of pristine P(VDF-HFP) (U_{dis} = 9.8 J cm⁻³), the U_{dis} of the NBT-P(VDF-HFP) composite film is improved by 58%. The resistivities and hopping conduction models of NBT-PEI and NBT-P(VDF-HFP) composite films (Supplementary Figs. 7 and 8 and Supplementary Note 1) show that the resistivities of

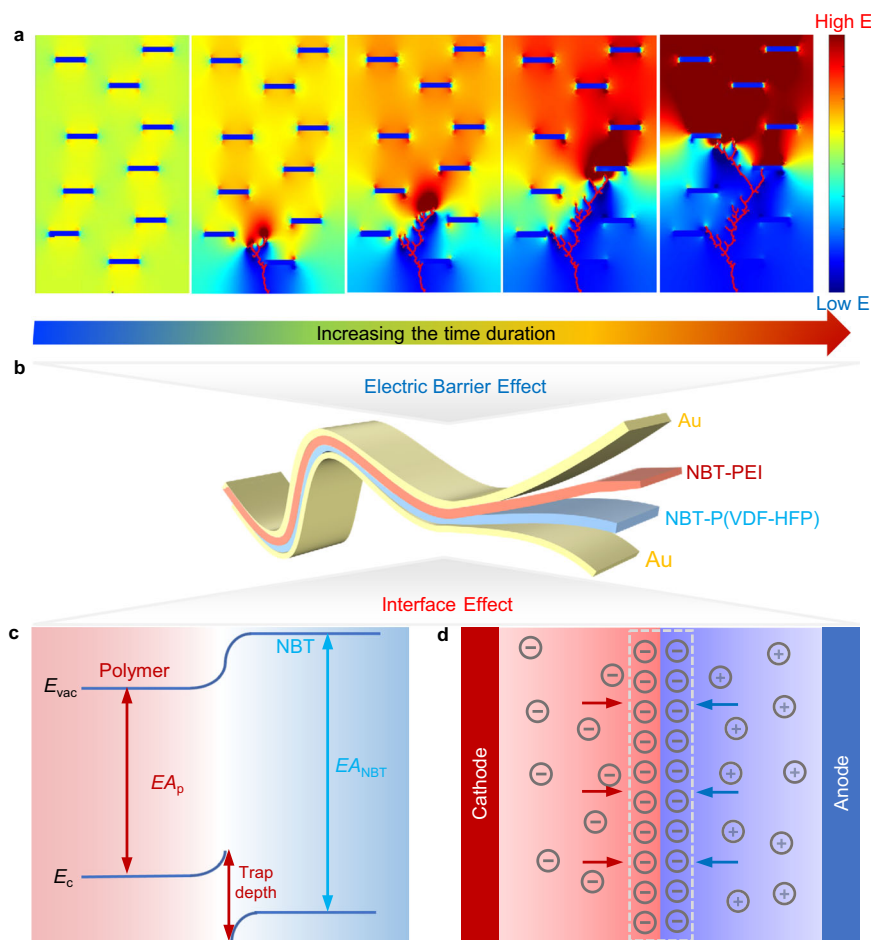


Fig. 1 | Schematic diagram of the designed bilayer-structured NBT-PEI/NBT-P(VDF-HFP) composites. **a** Simulation of the real-time evolving distributions of the electric field in NBT-polymer composites. **b** Schematic diagram of bilayer-structured composites. **c** Schematic diagram of the trap energy level caused by the

addition of the NBT sheets into composites. The trap energy level is calculated using $\Phi_e = EA_{\text{NBT}} - EA_p$, where EA_{NBT} and EA_p are electron affinities of the NBT sheets and the polymer, respectively. **d** Schematic diagram of the interface effect occurring in heterogeneous systems of PEI and P(VDF-HFP).

the NBT-PEI and NBT-P(VDF-HFP) slowly reduce with enhancing electric field compared to those of pristine PEI and P(VDF-HFP), and the charge hopping distances are reduced from 0.46 nm for PEI to 0.32 nm for NBT-PEI and from 0.48 nm for P(VDF-HFP) to 0.40 nm for NBT-P(VDF-HFP). These indicate that the additions of the 2D NBT sheets are of important value for causing the increase of the E_b in the NBT-PEI and NBT-P(VDF-HFP) composite films.

After the aforementioned optimization of the NBT filler content in the NBT-PEI and NBT-P(VDF-HFP) composite films, the bilayer-structured NBT-PEI/NBT-P(VDF-HFP) composite films are further designed and fabricated with three different structures: 3-7, 5-5 and 7-3 type composites, according to the thickness ratio of the NBT-PEI and NBT-P(VDF-HFP) layers. The optimized dielectric and capacitive properties are achieved in the 7-3 type composite film with an ultra-high E_b of 8283 kV cm⁻¹ (Supplementary Fig. 9, Supplementary Table 3 and Supplementary Note 2). Finite element simulations are used to study the electric potential and electric field distributions of the three different types of bilayer-structured composites at 6000 kV cm⁻¹ (Supplementary Fig. 10). The distributions of the electric potential and electric field tend to become more uniformly as the NBT-PEI layer content increases, which is beneficial for avoiding localized areas of high potential and reducing the risk of localized dielectric breakdown. Figure 3 shows the summarized dielectric and capacitive performance parameters of above optimized composites. As shown in Fig. 3a, the NBT-PEI/NBT-P(VDF-HFP) composite film has a medium ϵ_r of 5.0 and a low $\tan \delta$ of 0.02 at 1 kHz. In addition, the ϵ_r decreases little at high

frequencies, which is attributed to the introduction of PEI with a rigid molecular structure. Figure 3b shows the E_b of different kinds of composites obtained via the following Weibull distribution functions³³:

$$X_i = \ln(E_i) \quad (2)$$

$$Y_i = \ln(-\ln(1 - i/(n+1))) \quad (3)$$

In this context, n and i represent the total number of samples and the index of each individual sample, respectively, whereas E_i denotes the breakdown electric field for each sample. The slope of the fitted linear relationship between X_i and Y_i , known as the shape parameter (β), serves as an indicator of the reliability of the breakdown electric field (E_b) measurements. A higher β corresponds to greater reliability of the experimental data. The E_b is determined as the intersection of the linear fit with $Y_i = 0$. Notably, the minimum β for the NBT-PEI composite film is 16.4, underscoring the high quality and consistency of these composite films. The E_b massively increases from 4986 kV cm⁻¹ for pristine P(VDF-HFP) to 6084 kV cm⁻¹ for NBT-P(VDF-HFP) composite film when the 2D NBT sheets are introduced. Moreover, the E_b further enhances to 8283 kV cm⁻¹ by designing the bilayer structure. Compared with those of pristine P(VDF-HFP), the $D-E$ loops of the NBT-PEI/NBT-P(VDF-HFP) composite film are slimmer owing to the NBT-PEI layer with low D_r , as shown in Fig. 3c. Therefore, the NBT-

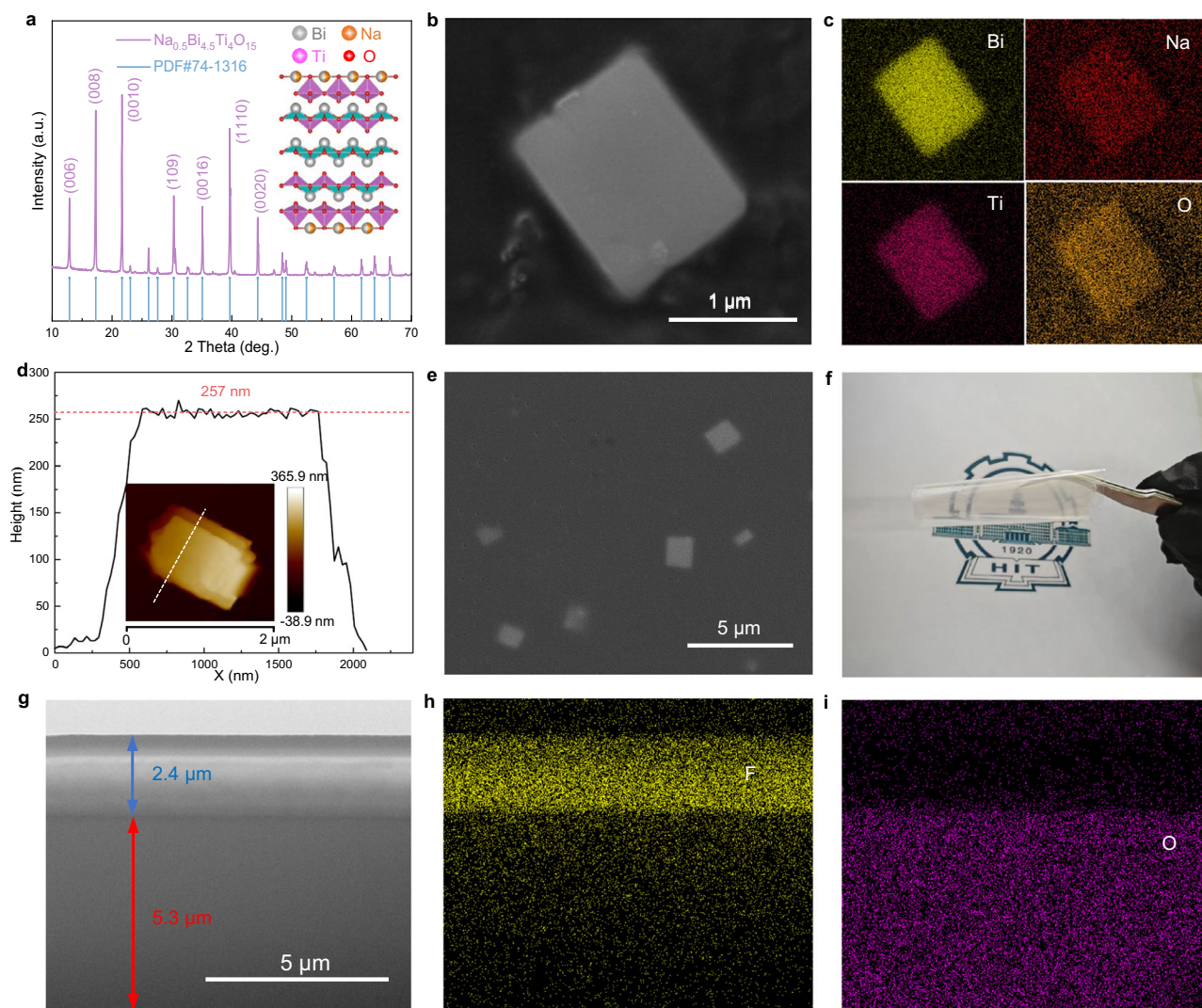


Fig. 2 | Characterization of NBT sheets and composite films. **a** XRD pattern and phase structure of 2D NBT sheets. **b** SEM image and **c** EDS mapping images of Bi, Na, Ti, and O in an NBT sheet. **d** Atomic force microscopy (AFM) image of a single NBT sheet. **e** Local surface SEM image and **f** Macroscopic digital photograph of the

bilayer-structured NBT-PEI/NBT-P(VDF-HFP) composite film. **g** FIB-SEM image, and EDS mapping images of **h** F and **i** O in the cross-section of NBT-PEI/NBT-P(VDF-HFP).

PEI/NBT-P(VDF-HFP) composite film exhibits the highest U_{dis} of 25.0 J cm^{-3} , accompanied by a high η of 81.2%, as plotted in Fig. 3d. To demonstrate the merits of this composite for dielectric capacitor applications, we summarize capacitive performances of the previously reported advanced composites^{8,29,34–46} in Fig. 3e (Supplementary Table 4). As observed, it is challenging to achieve large U_e and η in a kind of composite. For example, the BaTiO_3 -PVDF/PEI has a relatively high η of 84.5%, but the U_{dis} of 8.0 J cm^{-3} is low³⁶. The BaTiO_3 /PVDF has a high U_{dis} of 19.1 J cm^{-3} , but the η of 68.6% is low³⁷. Interestingly, in this study, by introducing 2D bismuth layer-structured NBT micro-sheets and designing the unique bilayer structure, a large U_{dis} of 25.0 J cm^{-3} and a high η of 81.2% are simultaneously achieved in the NBT-PEI/NBT-P(VDF-HFP) composite film.

Interface effect

The substantial enhancement in E_b can be partially attributed to the interface effect, which typically occurs in heterogeneous systems and is particularly pronounced if the constituent phases exhibit obviously different properties (e.g., ϵ_r , electron affinity, and band gap)⁴⁷. To elucidate the interface effect between the NBT micro-sheets and the surrounding polymers, energy band

diagrams at the PEI/NBT and P(VDF-HFP)/NBT interfaces (Fig. 4a, b) were constructed based on the ultraviolet photoelectron spectroscopy (Supplementary Figs. 11–13 and Supplementary Notes 3 and 4) and UV-Vis spectroscopy (Supplementary Figs. 14 and 15) results. As plotted in Fig. 4a, b, the NBT micro-sheets possess much higher electron affinity (EA_{NBT} , e.g., 6.2 eV) than both PEI (EA_1 , e.g., 2.8 eV) and P(VDF-HFP) (EA_2 , e.g., 2.4 eV), which causes the formation of deep trap energy levels ($\Phi_{e1} = EA_{\text{NBT}} - EA_1$, e.g., 3.4 eV, and $\Phi_{e2} = EA_{\text{NBT}} - EA_2$, e.g., 3.8 eV) to capture injected and excited electrons through strong electrostatic attraction. As a result, E_b is effectively enhanced. Furthermore, to further study the interface effect between NBT-PEI and NBT-P(VDF-HFP), the space charge development in the NBT-PEI/NBT-P(VDF-HFP) composite film were measured via the pulsed-electroacoustic (PEA) test (Fig. 4c, d). By integrating the interface space charge peak, the obtained interface charge density at 300 kV cm^{-1} is $1.13 \times 10^{-3} \text{ C m}^{-3}$ (Fig. 4d and Supplementary Note 5), which is much higher than the MWS theoretical value ($3.29 \times 10^{-3} \text{ C m}^{-2}$, Supplementary Note 5). As we know, MWS effect is only part of the interface effect. The higher interface charge density may suggest that a large amount of deep traps form in the

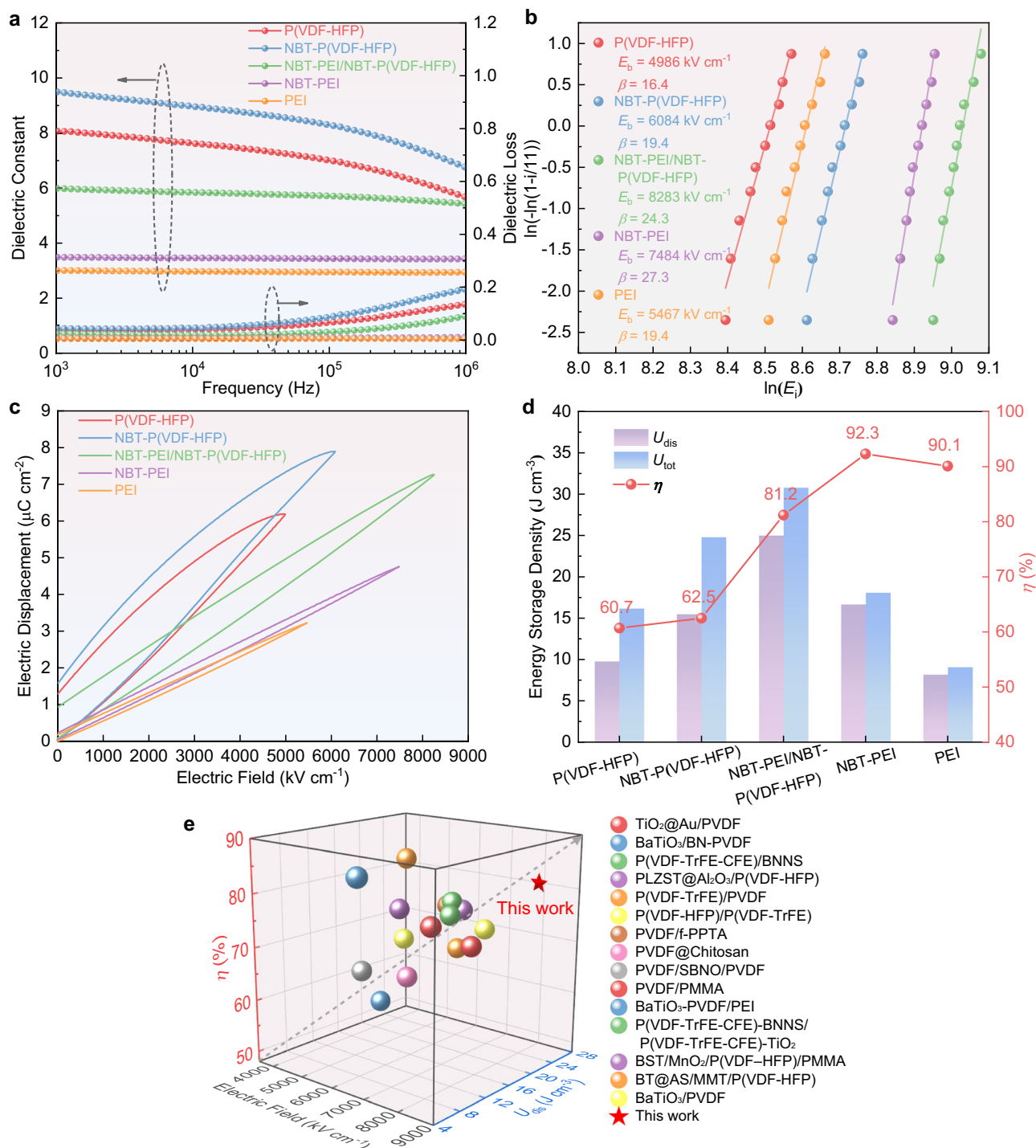


Fig. 3 | Dielectric and energy storage performance. **a** Frequency dependence of the ϵ' and $\tan \delta$. **b** Weibull distribution plots, **c** D - E loops and **d** U_{dis} , U_{tot} and η values of different types of composites. **e** Capacitive performances of previous reported advanced composites.

interface region of the bilayer-structured composite film, which also leads to a large accumulation of space charges⁴⁷. Such unique structure of the interface is believed to play an important role in enhancing the E_b . In addition, the resistivities and hopping conduction models of the NBT-PEI, NBT-P(VDF-HFP) and NBT-PEI/NBT-P(VDF-HFP) composite films (Fig. 4e,f) show that the resistivity of NBT-PEI/NBT-P(VDF-HFP) decrease slowly with increasing the electric field, and the charge hopping distance is decreased from 0.40 nm for NBT-P(VDF-HFP) composite film and 0.32 nm for NBT-PEI composite film to 0.30 nm for NBT-PEI/NBT-P(VDF-HFP) composite film. All above these results demonstrate that the

bilayer-structured NBT-PEI/NBT-P(VDF-HFP) composite film has significantly enhanced electrical breakdown resistance owing to the interface effect.

Finite element simulation of the real-time evolution of the electric potential and electric field distribution

To further investigate the enhancement mechanism for E_b , the real-time distribution evolving of the electric potential and electric field in the pristine PEI, NBT-PEI, and NBT-PEI/NBT-P(VDF-HFP) composite films were simulated at 7000 kV cm^{-1} via COMSOL Multiphysics and MATLAB (Fig. 5, Supplementary, Fig. 16 and Supplementary Note 6).

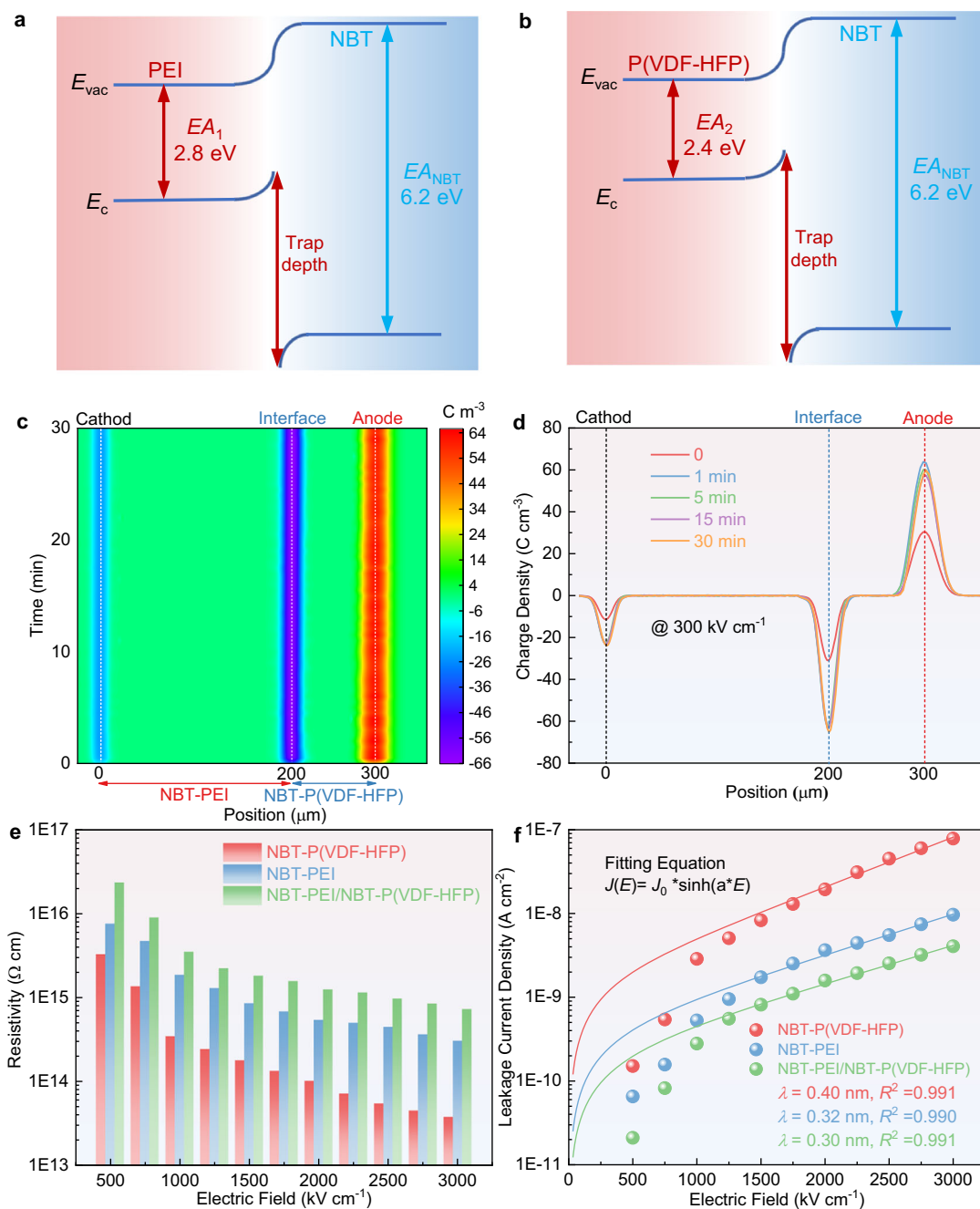


Fig. 4 | Interface effect. **a** Energy band diagrams at the NBT/PEI interfaces and **b** NBT/P(VDF-HFP) interfaces, where EA_1 , EA_2 , and EA_{NBT} respectively represent electron affinities of PEI, P(VDF-HFP), and NBT sheets, E_{vac} and E_c are vacuum level and conduction band. **c**, **d** Space charge density development under 300 kV cm^{-1} in

the 7-3 type composite film as functions of the position and time. **e** Resistivity and **f** leakage current density of the NBT-P(VDF-HFP), NBT-PEI, and NBT-PEI/NBT-P(VDF-HFP) composite films at various electric fields.

As shown in Fig. 5a, because pristine PEI has a monolithic structure, it has no difference in the overall electric field distribution, which leads to the preferential growth pathway of electric dendrites along the direction of the applied electric field. Consequently, the electrical trees show few branches and little energy loss during the evolution process, which leads to quick growth of electrical trees to the top boundary. In contrast, as shown in Fig. 5b, the introduction of 2D NBT sheets changes the distributions of the electric field in the NBT-PEI composite film. To be specific, a localized high electric field region is formed around the 2D NBT sheets, and the differences of the electric field between the tips of the electrical trees and the NBT is small. Therefore,

the electrical trees tend to produce more branches toward the surrounding low electric field regions. Consequently, the tortuous growth path of electrical trees and the appearance of many electrical tree branches lead to a large energy loss during their evolution process. Furthermore, as shown in Fig. 5c, the electric field distribution is dramatically changed via designing the bilayer structure with a clear demarcation formed at the interface. When electrical trees pass through the interface, the appearance of much lower electric field regions near such interface makes the electrical trees prone to produce more branches. Therefore, more energy loss occurs during the evolution process. All these effects slow down the development of

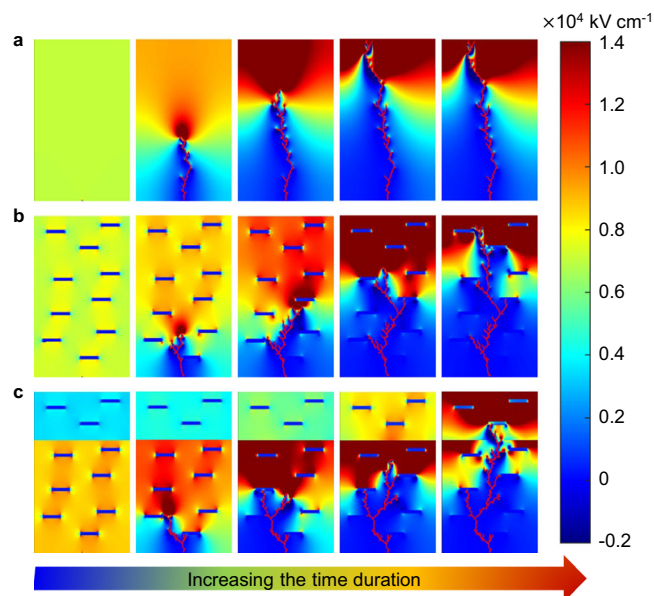


Fig. 5 | Simulation of the real-time evolution of the electric field distribution. **a** Pristine PEI, **b** NBT-PEI composite film and **c** NBT-PEI/NBT-P(VDF-HFP) composite film.

electrical trees at the upper boundary, leading to a substantial enhancement in the E_b .

Charge-discharge capacity

Compared with energy storage properties, the practical charge-discharge characteristics for dielectric capacitors are also critical for the application purpose. Hence, the underdamped and overdamped discharge properties of the NBT-PEI/NBT-(PVDF-HFP) composite film are tested through a discharge resistance, inductance, and capacitance load (RLC) circuit^{48–50}. Underdamped pulsed discharge current, the maximum current (I_{\max}) and current density ($C_D = I_{\max}/S$, where S is the electrode area) of the NBT-PEI/NBT-(PVDF-HFP) composite film at various electric fields are shown in Figure 6a, b. As presented, the composite film possesses an I_{\max} of 51.5 A and an ultra-high C_D of 102.5 A cm⁻² at 3000 kV cm⁻¹. Figure 6c, d shows the discharge energy density (W_d) at different electric fields, which is calculated by the following equation^{48–50}:

$$W_d = \frac{R \int I(t)^2 dt}{V} \quad (4)$$

Where V , I , and R are the sample volume, the discharge current acquired by overdamped charge-discharge tests, and the load resistor ($R = 300 \Omega$), respectively. Typically, the parameter $t_{0.9}$, which means the time required for releasing 90% of the W_d , can characterize the discharged rate of a material. The NBT-PEI/NBT-(PVDF-HFP) composite film presents a rapid discharge rate of 46.6 ns, a large W_d of 2.9 J cm⁻³ and an ultra-high power density (P_D , $P_D = W_d/t_{0.9}$) of 62.2 MW cm⁻³ at 3000 kV cm⁻¹. Figure 6e displays the W_d of NBT-PEI/NBT-(PVDF-HFP) composite film at 3000 kV cm⁻¹ when the cycle number is increased from 1 to 10³. As shown, W_d varies in the range of 2.74 to 3.01 J cm⁻³, indicating good fatigue resistance. Encouragingly, as illustrated in Fig. 6f, compared with previously reported advanced composites^{34,35,39,40,51–54}, our bilayer-structured composite film has both a much higher power density and a faster discharge rate, demonstrating very promising application potential in high pulsed power devices.

In summary, we have successfully prepared an attractive NBT-PEI/NBT-P(VDF-HFP) composite film by integrating 2D ferroelectric NBT

micro-sheets and bilayer structure, which can significantly increase the E_b of the composite films. Specifically, adding 0.75 wt.% NBT filler increases the E_b from 5467 kV cm⁻¹ for pristine PEI to 7484 kV cm⁻¹ for the NBT-PEI composite film. The designed bilayer structure further proves positive effect in boosting the E_b of composite films. The large interface charge density of 1.13×10^{-2} C m⁻² obtained from the PEA test indicates that the further improvement in the E_b is due to the interface effect. Moreover, optimizing the thickness ratio of NBT-PEI to NBT-P(VDF-HFP), the NBT-PEI/NBT-P(VDF-HFP) bilayer-structured composite film exhibits an ultra-high E_b of 8283 kV cm⁻¹, resulting in an ultra-high U_{dis} of 25.0 J cm⁻³ and large η of 81.2%. Besides, the composite film possesses an ultra-high power density of 62.2 MW cm⁻³ and a fast discharge rate of 46.6 ns. Compared with previously reported advanced composites, both high energy storage density and efficiency are realized in our bilayer-structured composite film. This study provides a novel strategy for developing high-performance polymer-based energy storage materials.

Methods

Preparation of 2D bismuth layer-structured NBT sheets

Na_{0.5}Bi_{4.5}Ti₄O₁₅ sheets were prepared via a molten salt growth method. Na₂CO₃ (99.5%, Aladdin, Shanghai, China), Bi₂O₃ (≥99.9%, Aladdin), and TiO₂ (≥99.0%, Aladdin) were used as raw materials, NaCl (≥99.5%, Aladdin, Shanghai, China) was used as molten salt. All materials were weighed based on the weight ratio of raw material: molten salt = 1:15 and mixed via ball-milling in ethanol for 24 h. The mixtures were calcined at 850 °C for 1 h to fabricate fine-grain matrix, and the excess impurities were washed away. Finally, 2D NBT sheets with the size of approximately 1–2 μm were obtained after drying.

Fabrication of NBT-P(VDF-HFP) and NBT-PEI composites

NBT-PEI composites were fabricated by a casting method, PEI (PolyK, USA) pellets were introduced into N-methyl pyrrolidone (NMP) (Macklin, 99.5%) solvent by stirring for 4 h to obtain transparent PEI solution. At the same time, the 2D NBT sheets were also distributed in NMP solvent by ultrasonically stirring for 20 min. Then, the above two solutions were mixed together and stirred for 12 h at room temperature to achieve uniform dispersion of NBT sheets. The solution was then cast onto a glass substrate by casting machine and dried at 70 °C for 12 h in vacuum oven to volatilize the NMP. The NBT-PEI composites with a thickness of approximately 7–10 μm were stripped from the glass substrate, and covered with Au electrodes with the diameter of 2 mm. Similar to the fabrication of NBT-PEI composites, the NBT-P(VDF-HFP) composites were successfully obtained and covered with Au electrodes with a diameter of 2 mm for the measurement of electrical performances.

Fabrication of bilayer-structured NBT-PEI/NBT-P(VDF-HFP) composite films

The NBT-PEI/NBT-P(VDF-HFP) composite film was fabricated by layer-by-layer casting from the prepared NBT-PEI and NBT-P(VDF-HFP) solutions. First, the NBT-PEI solution was cast on a glass substrate and dried at 70 °C for 12 h in vacuum as the bottom film. The NBT-P(VDF-HFP) solution was subsequently cast on the NBT-PEI film at 70 °C for 12 h in vacuum as the top film, because the PEI matrix is a thermosetting polymer and not dissolvable in the NBT-P(VDF-HFP) solution. Finally, three different types of NBT-PEI/NBT-P(VDF-HFP) composite films with different thickness ratios of the two layers, i.e., 0.7NBT-PEI/0.3NBT-P(VDF-HFP) (7-3 type), 0.5NBT-PEI/0.5NBT-P(VDF-HFP) (5-5 type) and 0.3NBT-PEI-0.7NBT-P(VDF-HFP) (3-7 type) composite films, were successfully prepared.

Characterization

X-ray diffraction (XRD, D/max 2400, Rigaku, Tokyo, Japan) was used to determine the phase structure. The microstructure and chemical

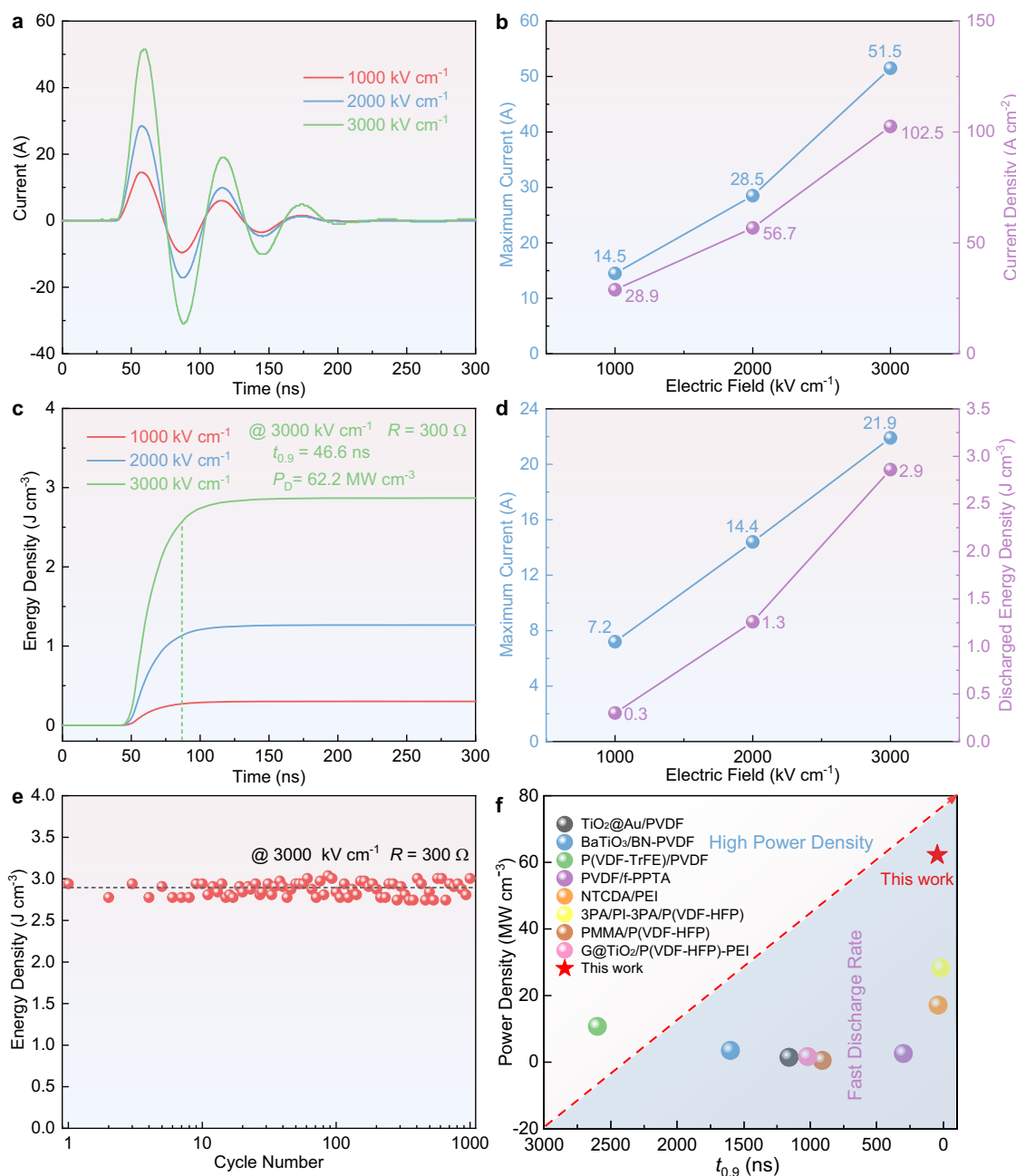


Fig. 6 | Charge-discharge capacity. **a** Underdamped pulsed discharge current. **b** Maximum current and current density under different electric fields. **c** Discharge energy density acquired by the overdamped charge-discharge test. **d** Maximum

current and discharge energy density under various electric fields. **e** Discharge energy density at different cycle numbers and 3000 kV cm⁻¹. **f** Charge-discharge performances of previously reported advanced composites.

composition were determined via field-emission scanning electron microscopy (FE-SEM, Merlin Compact, Germany) equipped with energy-dispersive spectroscopy (EDS). Cross-sectional images were measured via focused ion beam scanning electron microscopy (FIB-SEM, ZEISS Crossbeam 540, Helios G4 PFIB Hxe, Helios 600i). The thicknesses of the 2D sheets were measured via atomic force microscopy (AFM, Dimension Fastscan, Bruker, Germany). The dependences of the dielectric constant and loss on the frequency were obtained with a TH 2827 A precision LCR meter (Tonghui Electronic Co., Ltd., China). The E_b was achieved by the NJC5010 withstand voltage tester (Gogo Instruments Technology, China). The D - E loops, leakage currents, and resistivities at different electric fields were acquired with a Precision LC II ferroelectric testing system (Radiant Technologies Inc., USA). The

energy levels were tested by ultraviolet photoelectron spectroscopy (UPS, Thermo Fisher Scientific Nexsa G2, USA). The band gaps were determined via UV-Vis spectroscopy (Hitachi UH4150, Japan). The space charge distributions were tested by the pulsed-electro-acoustic (PEA, HY-PEA-DPT01, China) method. Discharge resistance, inductance, and capacitance (RLC) load circuit (CFD-003, Gogo Instruments Technology, China) were used to analyze the charge-discharge performance.

Data availability

All data supporting this study and its findings are available within the article and its Supplementary Information. The data corresponding to this study are available from the corresponding authors upon request.

References

- Chen, J. et al. Ladderphane copolymers for high-temperature capacitive energy storage. *Nature* **615**, 62–66 (2023).
- Yang, M. et al. Roll-to-roll fabricated polymer composites filled with subnanosheets exhibiting high energy density and cyclic stability at 200 °C. *Nat. Energy* **9**, 143–153 (2024).
- Zhou, J. et al. High-temperature dielectric energy storage films with self-co-assembled hot-electron blocking nanocoatings. *Nano Energy* **120**, 109184 (2024).
- Li, J. et al. Grain-orientation-engineered multilayer ceramic capacitors for energy storage applications. *Nat. Mater.* **19**, 999–1005 (2020).
- Li, R. et al. Giant dielectric tunability in ferroelectric ceramics with ultralow loss by ion substitution design. *Nat. Commun.* **15**, 3754 (2024).
- Singh, M., Tiwary, S. K. & Karim, A. Sub-nano fillers for high-temperature storage. *Nat. Energy* **9**, 113–114 (2024).
- Khanchaitit, P. et al. Ferroelectric polymer networks with high energy density and improved discharged efficiency for dielectric energy storage. *Nat. Commun.* **4**, 2845 (2013).
- Li, Q. et al. Solution-processed ferroelectric terpolymer nanocomposites with high breakdown strength and energy density utilizing boron nitride nanosheets. *Energy Environ. Sci.* **8**, 922–931 (2015).
- Bao, Z. et al. Negatively charged nanosheets significantly enhance the energy-storage capability of polymer-based nanocomposites. *Adv. Mater.* **32**, e1907227 (2020).
- Pan, Q. et al. 2D MXene-containing polymer electrolytes for all-solid-state lithium metal batteries. *Nanoscale Adv.* **1**, 395–402 (2019).
- Zhu, T. et al. Ultrahigh energy storage density in poly(vinylidene fluoride)-based composite dielectrics via constructing the electric potential well. *Adv. Energy Mater.* **13**, 2203587 (2023).
- Bera, S. et al. 2D-nanofiller-based polymer nanocomposites for capacitive energy storage applications. *Small Sci.* **3**, 2300016 (2023).
- Liu, X. et al. Charge-ferroelectric transition in ultrathin $\text{Na}_{0.5}\text{Bi}_{4.5}\text{Ti}_4\text{O}_{15}$ flakes probed via a dual-gated full van der Waals transistor. *Adv. Mater.* **32**, 2004813 (2020).
- Wang, C. M. et al. Electromechanical properties of -site (LiCe)-modified sodium bismuth titanate ($\text{Na}_{0.5}\text{Bi}_{4.5}\text{Ti}_4\text{O}_{15}$) piezoelectric ceramics at elevated temperature. *J. Appl. Phys.* **105**, 094110 (2009).
- Ma, Y. Q. et al. Topochemical synthesis and structural characteristics of orientation-controlled $(\text{Bi}_{0.5}\text{Na}_{0.5})_{0.94}\text{Ba}_{0.06}\text{TiO}_3$ perovskite microplatelets. *Microstructures* **2**, 2022006 (2022).
- Yao, Z. et al. Thermal stability and enhanced electrical properties of Er^{3+} -modified $\text{Na}_{0.5}\text{Bi}_{4.5}\text{Ti}_4\text{O}_{15}$ lead-free piezoelectric ceramics. *RSC Adv.* **6**, 94870–94875 (2016).
- Xie, H. et al. Enhanced energy storage properties under low electric fields in $(\text{Bi}_{0.5}\text{Na}_{0.5})\text{TiO}_3$ -based relaxor ferroelectrics via a synergistic optimization strategy. *Chem. Eng. J.* **450**, 138432 (2022).
- Fida, R. et al. Dielectric relaxation and conduction behaviors of Aurivillius $\text{Na}_{0.5}\text{Bi}_{4.5}\text{Ti}_4\text{O}_{15}$ ceramics with Na doping. *Rare Met.* **40**, 1247–1254 (2021).
- Long, C. et al. New layer-structured ferroelectric polycrystalline materials, $\text{Na}_{0.5}\text{Nd}_{1-x}\text{Bi}_{4.5-x}\text{Ti}_4\text{O}_{15}$: crystal structures, electrical properties and conduction behaviors. *J. Mater. Chem. C* **3**, 8852–8864 (2015).
- Jiang, C. et al. Topochemical transformation of two-dimensional single crystalline $\text{Na}_{0.5}\text{Bi}_{0.5}\text{TiO}_3$ - BaTiO_3 platelets from $\text{Na}_{0.5}\text{Bi}_{4.5}\text{Ti}_4\text{O}_{15}$ precursors and their piezoelectricity. *J. Mater. Chem. A* **5**, 15780–15788 (2017).
- Yang, M. et al. Surface engineering of 2D dielectric polymer films for scalable production of high-energy-density films. *Prog. Mater. Sci.* **128**, 100968 (2022).
- Chang, Y. et al. Fabrication of highly textured fine-Grained α -alumina by templated grain growth of nanoscale precursors. *J. Am. Ceram. Soc.* **96**, 1390–1397 (2013).
- Zhang, T. et al. Recent progress in polymer dielectric energy storage: from film fabrication and modification to capacitor performance and application. *Prog. Mater. Sci.* **140**, 101207 (2023).
- Hu, P. et al. Topological-structure modulated polymer nanocomposites exhibiting highly enhanced dielectric strength and energy density. *Adv. Funct. Mater.* **24**, 3172–3178 (2014).
- Liang, X. et al. BaTiO_3 internally decorated hollow porous carbon hybrids as fillers enhancing dielectric and energy storage performance of sandwich-structured polymer composite. *Nano Energy* **68**, 104351 (2020).
- Lin, Y. et al. Ultrahigh discharge efficiency and high energy density in sandwich structure $\text{K}_{0.5}\text{Na}_{0.5}\text{NbO}_3$ nanofibers/poly(vinylidene fluoride) composites. *Adv. Mater. Interface* **7**, 2000033 (2020).
- Yuan, C. et al. Polymer/molecular semiconductor all-organic composites for high-temperature dielectric energy storage. *Nat. Commun.* **11**, 3919 (2020).
- Gao, M. et al. Stiffness variable polymers comprising phase-changing side-chains: material syntheses and application explorations. *Adv. Mater.* **34**, 2109798 (2022).
- Jiang, Y. et al. Energy density and efficiency of scalable polymer nanocomposites utilizing core-shell PLZST/ Al_2O_3 antiferroelectric fillers with dielectric gradient. *Chem. Eng. J.* **446**, 136925 (2022).
- Yang M., et al. Unifying and suppressing conduction losses of polymer dielectrics for superior high-temperature capacitive energy storage. *Adv. Mater.* e2309640 (2023).
- Dou, L. et al. High-entropy-nanofibers enhanced polymer Nanocomposites for high-performance energy storage. *Adv. Energy Mater.* **13**, 2203925 (2023).
- Sharma, V. et al. Rational design of all organic polymer dielectrics. *Nat. Commun.* **5**, 4845 (2014).
- Fan, Z. et al. Ultra-superior high-temperature energy storage properties in polymer nanocomposites via rational design of core-shell structured inorganic antiferroelectric fillers. *J. Mater. Chem. A* **11**, 7227–7238 (2023).
- Ren Z., et al. Core-shell TiO_2 @Au nanofibers derived from a unique physical coating strategy for excellent capacitive energy storage nanocomposites. *Adv. Funct. Mater.* **34**, 2401907 (2024).
- Guo, R. et al. Bilayer structured PVDF-based composites via integrating BaTiO_3 nanowire arrays and BN nanosheets for high energy density capacitors. *Chem. Eng. J.* **437**, 135497 (2022).
- Zhang, B. et al. Outstanding discharge energy density and efficiency of the bilayer nanocomposite films with BaTiO_3 -dispersed PVDF polymer and polyetherimide layer. *Chem. Eng. J.* **446**, 136926 (2022).
- Guo, R. et al. Significantly enhanced breakdown strength and energy density in sandwich-structured nanocomposites with low-level BaTiO_3 nanowires. *Nano Energy* **79**, 105412 (2021).
- Wei, W. et al. Design on polarization distribution in all-organic polymer hybrids for high density energy storage. *Chem. Eng. J.* **394**, 125052 (2020).
- Sun, X. et al. Gradient core-shell structure enabling high energy storage performances in PVDF-based copolymers. *J. Mater. Chem. A* **12**, 8216–8225 (2024).
- Zhang, Y. et al. High-energy-density all-organic dielectric film via a continuous preparation processing. *Adv. Funct. Mater.* **33**, 2300555 (2023).
- Che, J. et al. Inkjet printing of all aqueous inks to flexible micro-capacitors for high-energy storage. *Adv. Funct. Mater.* **33**, 231544 (2023).

42. Ryu, A. et al. Layer-controlled perovskite 2D nanosheet interlayer for the energy storage performance of nanocomposites. *Small* **19**, e2300526 (2023).
43. Wu, Q. et al. Poly(methyl methacrylate)-based ferroelectric/dielectric laminated films with enhanced energy storage performances. *Adv. Comp. Hybrid. Mater.* **5**, 1137–1144 (2022).
44. Shang, Y. et al. Double gradient composite dielectric with high energy density and efficiency. *J. Mater. Chem. A* **10**, 15183–15195 (2022).
45. Su, Y. et al. Energy storage properties of flexible dielectric composites containing $\text{Ba}_{0.4}\text{Sr}_{0.6}\text{TiO}_3/\text{MnO}_2$ heterostructures. *Chem. Eng. J.* **452**, 139316 (2023).
46. Luo, B. et al. Superhierarchical inorganic/organic nanocomposites exhibiting simultaneous ultrahigh dielectric energy density and high efficiency. *Adv. Funct. Mater.* **31**, 2007994 (2020).
47. Niu, Y. et al. Significantly enhancing the discharge efficiency of sandwich-structured polymer dielectrics at elevated temperature by building carrier blocking interface. *Nano Energy* **97**, 107215 (2022).
48. Zhang, L. et al. Decreasing polar-structure size: achieving superior energy storage properties and temperature stability in $\text{Na}_{0.5}\text{Bi}_{0.5}\text{TiO}_3$ -based ceramics for low electric field and high-temperature applications. *J. Eur. Ceram. Soc.* **41**, 5890–5899 (2021).
49. Chen, H. et al. Excellent energy storage properties and stability of $\text{NaNbO}_3\text{-Bi}(\text{Mg}_{0.5}\text{Ta}_{0.5})\text{O}_3$ ceramics by introducing $(\text{Bi}_{0.5}\text{Na}_{0.5})_{0.7}\text{Sr}_{0.3}\text{TiO}_3$. *J. Mater. Chem. A* **9**, 4789–4799 (2021).
50. Yang, F. et al. Realizing high comprehensive energy storage performances of BNT-based ceramics for application in pulse power capacitors. *J. Eur. Ceram. Soc.* **41**, 2548–2558 (2021).
51. Zhang, B. et al. Superior high-temperature energy density in molecular semiconductor/polymer all-organic composites. *Adv. Funct. Mater.* **33**, 2210050 (2022).
52. Pan, Y. et al. Excellent energy storage and discharge performances realized in polymer nanocomposites by introducing core-shell antiferroelectric fillers and constructing bilayer interfaces. *J. Alloy. Comp.* **969**, 172373 (2023).
53. Li, X. et al. All-polymeric multilayer para/ferroelectric dielectric films utilizing a gradient structure toward concurrent high discharge efficiency and energy density. *Mater. Today Energy* **29**, 101119 (2022).
54. Sun, L. et al. Concurrently Achieving high discharged energy density and efficiency in composites by introducing ultralow loadings of core-shell structured graphene@ TiO_2 nanoboxes. *ACS Appl. Mater. Interfaces* **14**, 29292–29301 (2022).

Acknowledgements

This work was financially supported by the National Natural Science Foundation of China (Nos. 52072092 (Y.F.C.), and 52372106 (Y.F.C)), the Natural Science Foundation of Heilongjiang Province (No. YQ2019E026 (Y.F.C)) and the Fundamental Research Funds for the Central Universities

(No. 2023FRFK03048 (Y.F.C)). The authors extend their gratitude to Shiyanjia Lab (www.shiyanjia.com) for the UPS measurement.

Author contributions

Z.H.F. and Y.F.C. conceived the idea. Z.H.F., D.W.W., and Y.F.C. designed the experiments. Z.H.F., J.D., H.X., Y.Y.H., Y.T.J., F.H., Y.Q.D., and W.F.Y. carried out the experiments. Z.H.F. performed the simulation. Z.H.F., D.W.W., and Y.F.C. analyzed the data. Z.H.F. drafted the manuscript. Q.F.Z., D.W.W., and Y.F.C. revised the manuscript. All authors discussed the results and commented on the manuscript.

Competing interests

The authors declare no competing interests.

Additional information

Supplementary information The online version contains supplementary material available at <https://doi.org/10.1038/s41467-024-55112-1>.

Correspondence and requests for materials should be addressed to Dawei Wang, Qingfeng Zhang or Yunfei Chang.

Peer review information *Nature Communications* thanks the anonymous reviewer(s) for their contribution to the peer review of this work. A peer review file is available.

Reprints and permissions information is available at <http://www.nature.com/reprints>

Publisher's note Springer Nature remains neutral with regard to jurisdictional claims in published maps and institutional affiliations.

Open Access This article is licensed under a Creative Commons Attribution-NonCommercial-NoDerivatives 4.0 International License, which permits any non-commercial use, sharing, distribution and reproduction in any medium or format, as long as you give appropriate credit to the original author(s) and the source, provide a link to the Creative Commons licence, and indicate if you modified the licensed material. You do not have permission under this licence to share adapted material derived from this article or parts of it. The images or other third party material in this article are included in the article's Creative Commons licence, unless indicated otherwise in a credit line to the material. If material is not included in the article's Creative Commons licence and your intended use is not permitted by statutory regulation or exceeds the permitted use, you will need to obtain permission directly from the copyright holder. To view a copy of this licence, visit <http://creativecommons.org/licenses/by-nc-nd/4.0/>.

© The Author(s) 2025